BUILD SIMUL (2016) 9: 43–52
DOI 10.1007/s12273-015-0235-6

Numerical investigation of particle transport characteristics in an isolated room with single-sided natural ventilation

Xinming Jin, Lijun Yang (✉), Xiaoze Du, Yongping Yang

Key Laboratory of Condition Monitoring and Control for Power Plant Equipments of Ministry of Education, School of Energy Power and Mechanical Engineering, North China Electric Power University, Beijing 102206, China

Abstract

Single-sided natural ventilation has been common in multi-family residential buildings. Current research usually presumes that the outdoor air is clean, which is not realistic under the outdoor pollution situations. In this study, the particle transport and airflow pattern in an isolated living room with the single-sided natural ventilation are numerically investigated by means of Eulerian drift-flux model combined with the Eulerian fluid method. The results indicate that larger wind speed does not necessarily achieve better ventilation effect and higher air change rate (ACH). At high wind speeds, the effect of wind direction on the room average concentration becomes more conspicuous. Small particles tend to disperse in the room more uniformly while large particles exhibit stratified distributions. The results would be useful for optimizing single-sided natural ventilation in buildings.

Keywords

single-sided,
ventilation,
particle transport,
Eulerian,
deposition

Article History

Received: 27 January 2015
Revised: 11May 2015
Accepted: 12 May 2015

1 Introduction

Nowadays, the rapid increase of populations and deficit of resources across the world have resulted in an urgent need for energy-conservation buildings (Angel et al. 2011). Natural ventilation as an energy-efficient way to refresh a room has drawn lots of attention of the building designers (da Graça et al. 2002). Generally, there are two kinds of natural ventilation, cross flow and single-sided. For cross ventilation, air flows through a room via the openings on different facades of the building. Nevertheless, in densely occupied cities, a small room may only have one external facade (Gao et al. 2008). Therefore, single-sided natural ventilation is widely adopted in large cities. For single-sided ventilation, the flow rate across the opening may depend on many issues. Larsen and Heiselberg (2007) presented a new design expression for single-sided ventilation considering the impact of wind directions on the ACH. Besides, Wilson and Kiel (1990) measured the single-sided ACH in a test house with the temperature difference between indoor and outdoor environments, finding that a larger outdoor wind speed did not necessarily mean a higher ACH. Furthermore, Gao et al. (2008) simulated the airflow patterns at various wind speeds between two vertically adjacent rooms, observed that the air exhausted from the lower room can re-entrain the upper one under the gentle wind conditions, while this effect can be suppressed by the strong wind.

From the aforementioned studies, single-sided natural ventilation is an ideal option for green buildings. However, most investigations assumed that outdoor air is clean. Possible influence of pollutants from outdoor environment on indoor air quality has not been taken into account (Li and Li 2015). However, the penetration of outdoor pollutants, especially the aerosol particles, can pose threat to human health. Dockery et al. (1993) and Chen et al. (2013) pointed out that air particle concentration is closely related to human mortality. So it is vital to study the particle transport and distribution in a room with the single-sided natural ventilation. The purpose of this paper is to clarify the transport characteristics of outdoor particles to an isolated room with the single-

E-mail: yanglj@ncepu.edu.cn

sided natural ventilation at various wind speeds and directions, which can be of benefit to the ventilation optimization of buildings.

2 Mathematical model

2.1 Turbulent airflow model

The steady state Navier–Stokes equations are solved to obtain the airflow patterns at four wind speeds and three different wind directions, and the interaction between the particles and fluid has been treated as one-way coupling, since the particle diameter of interest is so small that it can hardly impact the airflow field (Zhao et al. 2004). For the turbulent flow in the computational domain, the Reynolds average Navier–Stokes equations combined with Renormalization Group (RNG) k–ε model are employed (Launder and Spalding 1974). The general form of the governing equations can be expressed as

$$\nabla \cdot (\rho \vec{u} \varphi) = \nabla \cdot (\Gamma_\varphi \nabla \varphi) + S_\varphi \quad (1)$$

where $\vec{u}$ represents the time-averaged velocity; φ can be regarded as time-averaged velocity component (u, v, w); turbulent kinetic energy k; turbulent dissipation rate ε or air enthalpy h in different equations; Γ_φ and S_φ are the effective diffusivity and source term for each variable, respectively. The corresponding expressions can be found in the reference (ANSYS 2012).

A commercial CFD software FLUENT is used to solve Eq. (1) in the form of discretized algebraic equations with a second-order discretization scheme. The SIMPLE algorithm is adopted to couple the pressure and velocity fields. In order to take the buoyancy effect into consideration, the Boussinesq approximation is applied.

2.2 Particle phase model

In this study, the transport and deposition of particles are simulated with an Eulerian drift-flux model developed by Chen et al. (2006). Due to the feasibility of the proposed Eulerian model, the influences of other deposition mechanisms can be incorporated easily into the model. Another benefit of this model is the computational cost reduction since no individual particle tracking is required (Lai and Chen 2007). The governing equation of the particle phase takes the following form:

$$\nabla \cdot [(\vec{u} + \vec{v}_{s,i})] = \nabla \cdot [(D_i + \varepsilon_p) \nabla C_i] + Sc_i \quad (2)$$

where C_i is the particle mass concentration (kg/m^3) of the size group i, $\vec{v}_{s,i}$ is the particle gravitational settling velocity, which considers the relative velocity of the two phases. ε_p is the particle eddy diffusivity and D_i the Brownian diffusion coefficient. In the present simulation, particle sizes and velocities are so small that the assumption of $\varepsilon_p/\mu_t \approx 1$ can be used (Lai and Nazaroff 2000). A semi-empirical particle deposition model developed by Lai and Nazaroff (2000), which includes the structure of turbulent diffusivity in near-surface area of indoor environments, has been taken as a source term in the particle phase transport equation to deal with particle deposition on the walls.

2.3 Model validation

2.3.1 *Airflow around a bluff body*

Jiang et al. (2003) used wind tunnel tests to investigate the airflow pattern around an isothermal scaled room. The dimension of the room is $L(x) \times H(y) \times W(z) = 250$ mm $\times$ 250 mm $\times$ 250 mm, as shown in Fig. 1, with the wall thickness of 6 mm. In the experiment, the mean air velocity and its fluctuation were measured along 10 vertical lines at the middle plane of z direction with the laser Doppler anemometer. Four of these lines (shown in Fig. 2) are chosen in the present work to compare the numerical predictions with the experimental results. The geometry of the computational domain is $x \times y \times z = 13H \times 4H \times 9H$, the inlet

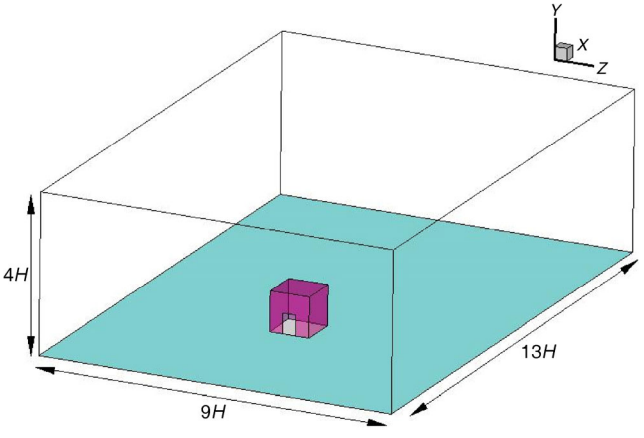

Fig. 1 Computational domain of the validation experiment

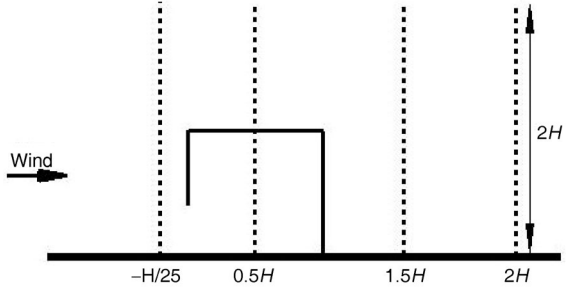

Fig. 2 Locations of four vertical lines on which numerical predictions and experimental measurements are compared

velocity profile in x direction followed $u_y = (u_0/\kappa)\ln(y/y_0)$ and the velocity components in other directions were zero. The isotropic Renormalization Group (RNG) k–ε model combined with wall functions are used to compute the turbulence in the domain. Comparisons between the experimental measurements and simulation results are illustrated in Fig. 3. It can be observed that, although the simulation results at the upper part of line $H/2$ and lower part of line $2H$ exhibit little deviations from the measurements, the overall data of present numerical model are satisfactory, which justifies the RNG k–ε model to be reliable enough to simulate airflow distribution in single-sided ventilation room in this study.

2.3.2 *Particle transport in a model chamber*

Chen et al. (2006) measured the distribution of the particle with a diameter of 10 μm in a model chamber. Figure 4 shows the geometry of the chamber, in which the air inlet and outlet (0.04 m × 0.04 m) are symmetrical about the middle plane y = 0.2 m. In the experiment, the particles are uniformly mixed with the supply air by a disperser and then injected into the chamber with a velocity of 0.45 m/s. Using the Eulerian drift-flux model mentioned above, the particle normalized concentrations on three lines (x = 0.2, 0.4 and 0.6 m) at the center plane are computed and compared with the experimental results as shown in Fig. 5. It can be seen that the maximum error appearing at the top region of x = 0.4 m between the experimental and simulation results is 39.84%, which can attribute to the inaccurate turbulence predicted by the RNG k–ε model in this study. The average errors for the three cases are 18.08%, 16.13% and 8.65% respectively. From the view of the computational accuracy and cost, the numerical model predicts the particle concentration well, so the same drift-flux model is applied to the particle transport simulation for the single-sided ventilation.

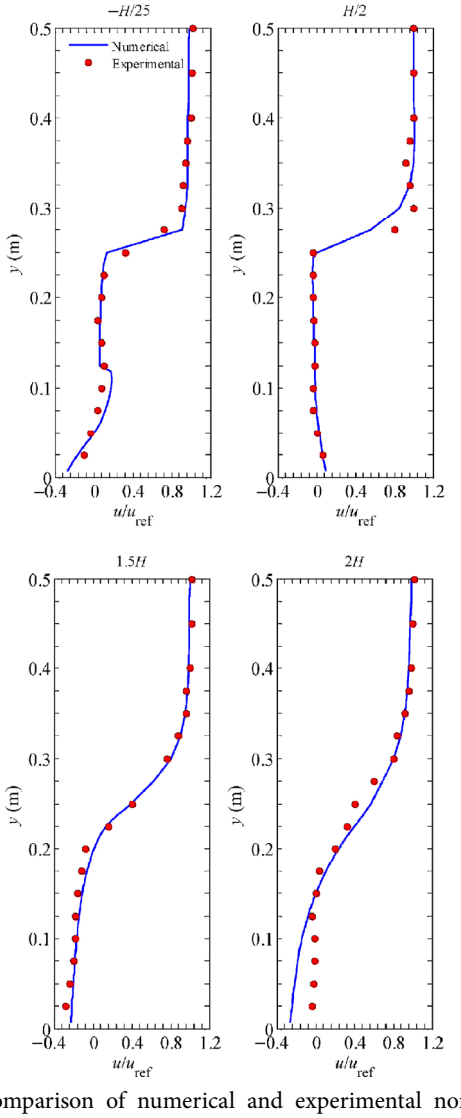

Fig. 3 Comparison of numerical and experimental normalized velocities on four vertical lines

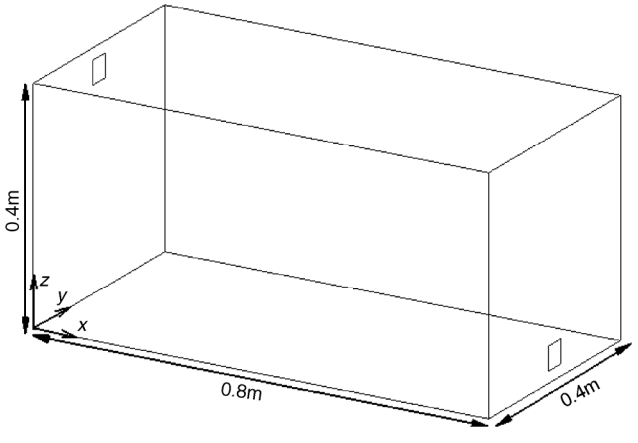

Fig. 4 Chamber geometry for the validation experiment

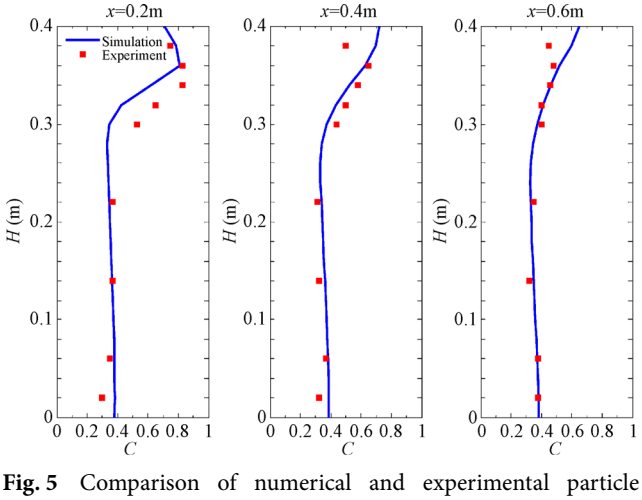

Fig. 5 Comparison of numerical and experimental particle normalized concentrations on three lines (x = 0.2, 0.4 and 0.6 m) in the middle plane of y direction

3 Case set-up

In order to investigate the particle transport characteristics in an isolated room with the single-sided ventilation, a typical living room with a man lying on the bed is chosen as shown in Fig. 6(a). The room dimensions are $H \times W \times L$ = 2.7 m × 3.2 m × 4 m and the bed geometric size is 1.2 m(x) × 0.5 m(y) × 2 m(z). The left side of the bed is on the middle plane in the x direction of the room. With a purpose of reducing computational cost, the head of manikin is simplified as a sphere with a diameter of 20 cm, and two circles with a diameter of 1 cm represent the manikin nose. The window at the front surface of the room is 1.6 m(y) × 1 m (z). In this study, three wind directions, normal, left 45° and right 45°, are investigated as shown in Fig. 6(b). The size of the computational domain is $x \times y \times z$ = 64.8 m × 20 m × 24.8 m, which is large enough to guarantee the accuracy of the simulation results. The cases in normal wind direction and in the direction of left 45° as a representative are shown in Fig. 7(a) and 7(b).

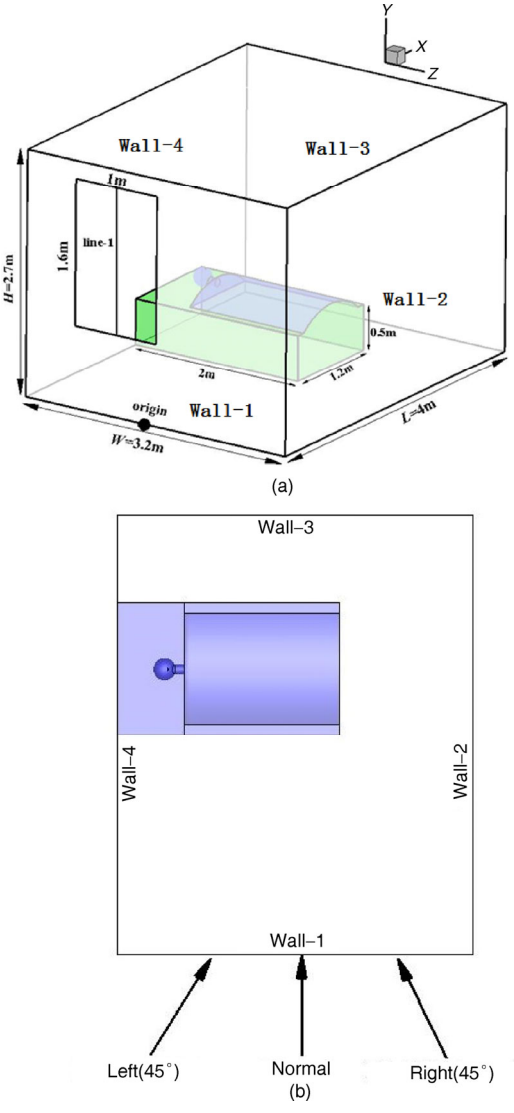

Fig. 6 Schematic of living room and wind directions: (a) living room, (b) wind direction

The inlet of computational domain is defined as the velocity boundary condition and four different wind profiles are selected to represent various environmental wind conditions. In the simulation of windless case, a uniform wind speed of 0.1 m/s is selected. The typical wind speed in the urban environment is usually larger than 0.1 m/s and follows a power law distribution as follows (Etheridge and Sandberg 1996):

$$u_y = 0.35 u_w y^{0.25} \tag{3}$$

where u_w is the wind speed measured at 10 m above the ground and y is the vertical distance. In this work, three wind profiles are taken into account (u_w=1 m/s, 2 m/s and 4 m/s) except the windless case. The turbulence boundary conditions are specified by the turbulence intensity and length scale, which are 8% and 1 m respectively as an illustrative case. The outlet is set as the pressure outlet condition and the lateral and upper surfaces of the domain are symmetrical.

Previous studies about natural ventilation have revealed the significant interactions between the approaching wind profile and indoor buoyancy effect (Zhao and Zeng 2009; Lo and Novoselac 2013; Ayo et al. 2015). Thus, the temperature difference between the outdoor and indoor environments is considered with the Boussinesq approximation. The temperature of the atmospheric environment is 293 K, while a

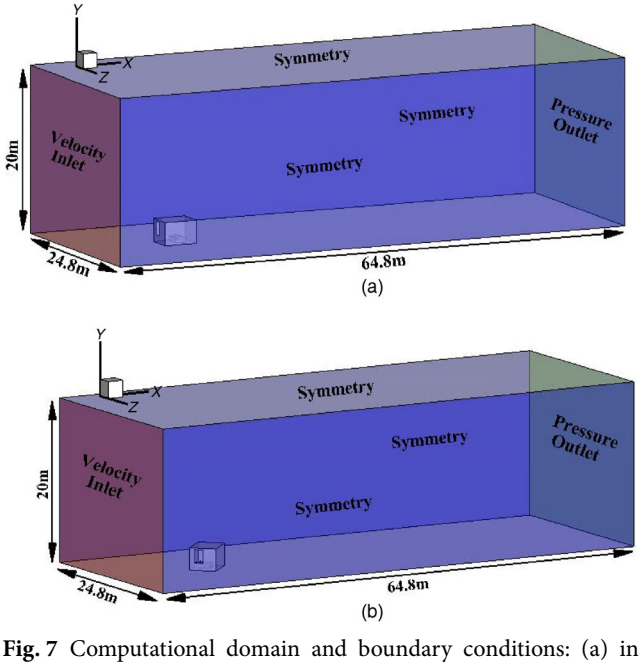

Fig. 7 Computational domain and boundary conditions: (a) in normal wind direction; (b) in the wind direction of left 45°

higher temperature is specified to the indoor environment. For the human body, a constant temperature of 304 K recommended by Gao and Niu (2004) is applied and the wall surfaces of the room are 298 K. Adiabatic boundary conditions are set to the surfaces of bed. The periodic respiration activity of human is treated as a steady inhalation according to (Hörschler et al. 2010). For each nostril, a constant inhalation rate of 7.5 litres per minute is applied, which represents the human breath at the light activity. Standard wall functions are applied to near-wall regions.

To obtain the steady particle distributions at various wind speeds and directions, an Eulerian drift-flux model considering gravitational settling is employed. The inlet particle concentration is specified as unity, that is to say, the particle concentrations within the domain are normalized with the inlet value. For particle deposition onto the indoor surfaces, a semi-empirical model developed by (Lai and Nazaroff 2000), which accounts for the effects of Brownian and turbulent diffusion and gravitational settling, is used as the boundary condition. The expression for the particle deposition flux, $J_{d,i}$ ($m^{-2}\cdot s^{-1}$), is given as (Chen et al. 2006):

$$J_{d,i} = v_{d,i} C_{b,i} \tag{4}$$

where $C_{b,i}$ is defined as the normalized bulk concentration of particles, which is taken as the concentration value in the first cell adjacent to the wall and can be treated as uniform. $v_{d,i}$ is the deposition velocity of particle. Besides, inhalable particle diameters of the indoor environment are usually less than 10 μm according to the review of (Nazaroff 2004), therefore, two typical diameters of 1 μm and 10 μm are selected to represent the small and large particles respectively.

In the process of calculation, the steady state airflow pattern is obtained by solving RANS equations with the solver FLUENT, then the drift-flux model is incorporated by the user defined scalar (UDS) module to compute the particle distributions in the steady airflow fields. A flow chart briefly describing the computational process is shown in Fig. 8. Moreover, ACH is computed with a tracer gas decaying method, in which the steady flow field has been solved at first, then the tracer gas (CO_2) was uniformly distributed in the room and the temporal evolution of volume-averaged indoor CO_2 concentration was calculated according to the steady airflow. The ACH can then be calculated according to Eq. (5) as follows, where C_0 represents the initial concentration of CO_2, C_τ is the transient concentration at the time τ. In this study, the ACH is computed according to the volume-averaged CO_2 concentration at $\tau = 600$ s.

$$\mathrm{ACH} = 3600 \times \ln\left(\frac{C_0}{C_\tau}\right) \times \frac{1}{\tau} \tag{5}$$

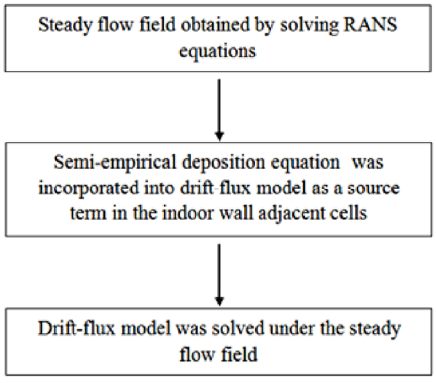

Fig. 8 Flow chart for the numerical simulation of particle transport characteristics

The mesh of the computational model was generated by the software GAMBIT 2.4.6. The computational domain is discretized by hexahedral elements with variable sizes. For regions inside and close to the room, the mesh is the finest with the interval size of 40 mm corresponding to a $y+$ value larger than 30, which justifies the application of the standard wall functions and the semi-empirical deposition model developed by Lai and Nazaroff (2000). A coarser resolution about 50–150 mm is employed in the regions far away from the room. The mesh details around the room in the normal wind direction are shown in Fig. 9(a) and similar

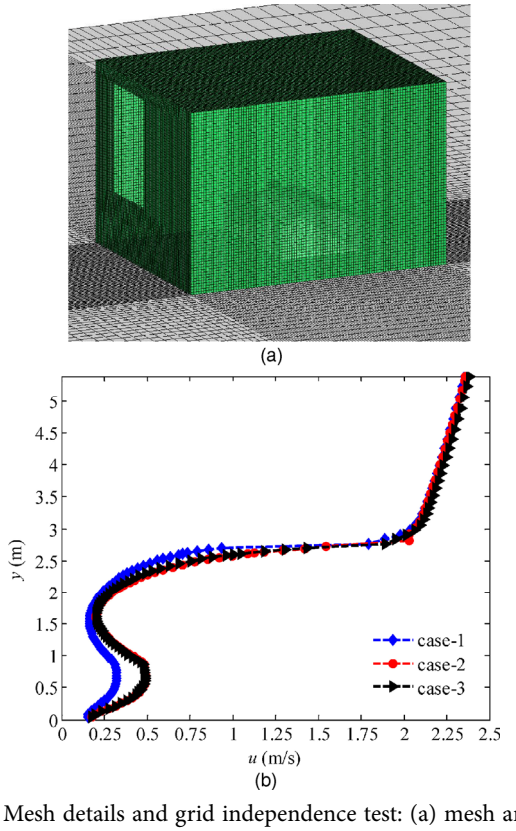

Fig. 9 Mesh details and grid independence test: (a) mesh around the room; (b) grid independence test by comparing the velocity magnitude

mesh generations are used in other two wind directions. The grid independence tests are done for various wind directions. In the normal wind direction, three numbers of cells, 2.5×10^6 (case-1), 4.3×10^6 (case-2) and 6.5×10^6 (case-3) are adopted to check the independence. Figure 9(b) shows the velocity magnitude at the line $x = -H/25$ in the plane of $z = 0$. It can be observed that the velocity in case-2 varies little with that in case-3, and can predict the airflow characteristics in the room well, so the case-2 with 4.3×10^6 cells is applied to the following simulations. In the wind directions of left 45° and right 45°, the final grid numbers of 5.8×10^6 and 5.9×10^6 are taken after the independence test.

The convergence criterion of 10^{-6} is applied for all the variables in the simulations. Besides, the area-weight average velocity magnitudes at several interior faces in the room are also monitored. After about 5000 iterations, the residuals and average velocities no longer decrease but are maintained at an acceptable level. Then the solutions are regarded as converged.

4 Results and discussion

Airflow patterns in the plane $z = -0.5$ m (line-1 is on this plane) at various wind speeds in the normal wind direction are shown in Fig. 10. In general, the cold outdoor air pours down to the room from the lower part of the opening and diffuses along the floor, displacing the indoor air and finally flows out from the upper part. This flow structure, which can be seen at relatively small wind speeds (u_w = 0.1 m/s, 1 m/s, 2 m/s), is mainly due to the buoyancy effect resulting from the temperature difference between the indoor and outdoor environments. With the increase of wind speed, however, the effective depth of fresh air decreases gradually, wakening the displacement effect of indoor air. When the speed arrives at 4 m/s, it is clearly observed that the indoor airflow is relatively calm, only a small portion of cold outdoor air enters into the room. Figure 11 compares the velocity components in the x direction at different heights of the middle line (line-1) for the case in the normal wind direction, in which the positive value represents flowing into the room while negative one indicates flowing out. A nearly identical velocity distribution is produced when the speeds are 0.1 m/s and 1 m/s. While the velocity magnitude at the speed of 2 m/s is smaller, but still maintaining the similar profile, that is, air entering into the room from the lower part, flowing out from the upper part. Nevertheless, totally different velocity distribution appears in the case of u_w = 4 m/s. The cold outdoor air gets into the room from the upper part while escapes from the lower part. This difference can be attributed to the interaction between the

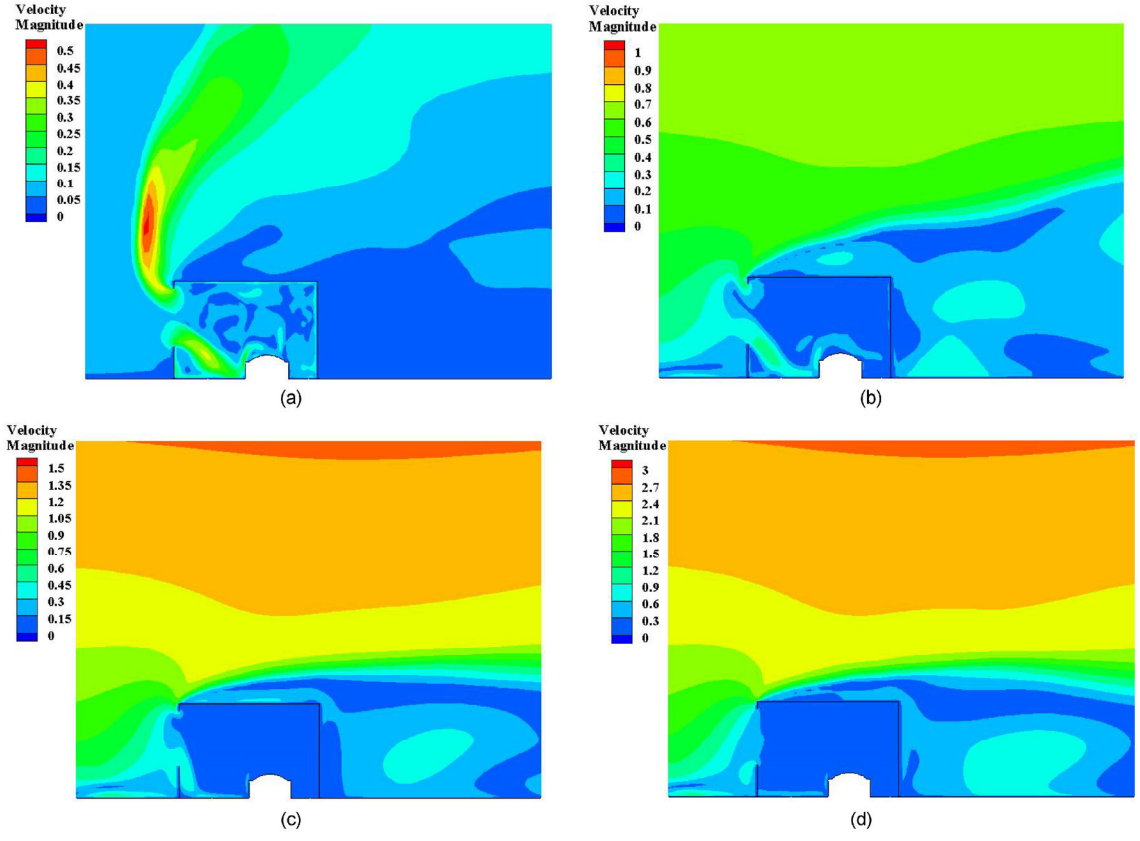

Fig. 10 Airflow patterns at four wind speeds in the normal wind direction (velocity unit in m/s): (a) 0.1 m/s; (b) 1 m/s; (c) 2 m/s; (d) 4 m/s

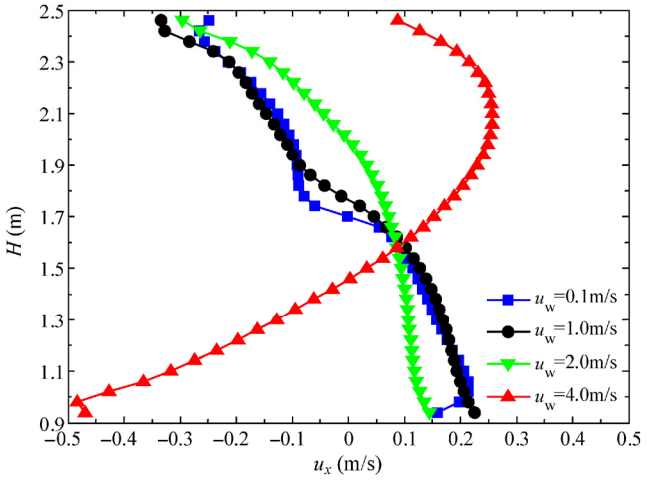

Fig. 11 Distributions of x velocity component on the middle line of the opening at various wind speeds in the normal wind direction

buoyancy effect and inflow wind profile. At the lower speeds (u_w = 0.1 m/s, 1 m/s), buoyancy effect dominates the flow structure. Cold outdoor air sinks and spreads over the floor, then absorbs heat from the indoor environment, escaping from the upper part of the opening. On the contrary, when the speed increases to 4 m/s, strong air mixing in the vicinity of the opening can be observed, which reduces the flow rate through the opening and results in a very limited effective depth of fresh air. Similar airflow patterns can be observed with different wind directions.

The changing trends demonstrated above accord with the experimental results of (Wilson and Kiel 1990), which observed that the ventilation rate generated by strong wind speed (5.5 m/s measured at 10 m above the ground) can be 25% smaller than the windless condition. The reason according to (Wilson and Kiel 1990) can be ascribed to the increased intensity of outdoor turbulence, which further increases the interfacial mixing at the near field of the opening and reduces the net ventilation rate. And moreover, the measurements of (Hunt and Linden 1999) indicated that ACH is relevant to the Froude number ($Fr = u/(g'h)^{1/2}$): the larger the number is, the smaller the ACH value is produced. In the present simulation, the case of u_w = 4 m/s in the normal wind direction can produce a Fr number of about 5, which is corresponding to a relatively low ACH. Besides, the approaching wind profile may attenuate the pressure difference near the opening, and turbulent fluctuations in the wind can further enhance the air mixing across the opening. As a result, the velocity magnitude in the vicinity of the opening is largest at the case of 4 m/s (shown in Fig. 11), but the corresponding indoor airflow is relatively calm and the ACH is similar to the windless condition.

Figure 12 compares the changes of normalized volume-averaged indoor CO_2 concentration and ACH at various wind speeds and in various wind directions. In the same direction, it can be observed that stronger wind speed does not necessarily mean lower CO_2 concentration and higher ACH. For the nearly windless one (u_w = 0.1 m/s) in the normal wind direction as shown in Fig. 12(a), the airflow is mainly affected by buoyancy force, resulting in an ACH of 8.64. When the speed increases to 1 m/s, CO_2 concentration decreases rapidly, corresponding to an ACH of 20.16 nearly three times bigger than the windless one. At the high speeds (u_w = 2 m/s and 4 m/s), however, CO_2 concentration decreases relatively slower than the case of u_w = 1 m/s and the ACH is similar to the windless case. As for the wind direction, it is shown that the ACH values of 1 m/s, 2 m/s and 4 m/s in the normal wind direction are conspicuously larger than those in the directions of left and right 45°, which can attribute to the reduced effective flow area near the opening and the enhanced interfacial air mixing in the non-normal directions. On the contrary, the ACHs at the low wind speed in the non-normal directions are larger than that in the normal wind direction, and the ACH in the wind direction of right 45° even arrives at 12.60, showing that the buoyancy effect dominates the airflow patterns in the non-normal wind directions.

Particle distributions with different diameters at the speeds of 1 m/s and 4 m/s in the normal wind direction are shown in Fig. 13. It can be seen that the particle concentration near the floor is higher than that on the ceiling, and the particle concentration with the diameter of 1 μm is larger than that with the diameter of 10 μm. Moreover, under the effect of Brownian and turbulent diffusion, small particles distribute more uniformly. Dominated by the gravitational settling effect, large particles accumulate in the lower part of the room, demonstrating stratified patterns. Figure 14 compares the particle deposition flux at different surfaces of the room at three typical urban wind speeds (1 m/s, 2 m/s and 4 m/s) and in three wind directions. In the same wind direction, the deposition flux exhibits similar distributions at different speeds, namely, the wind speed hardly affects the deposition flux. Additionally, the deposition fluxes at vertical surfaces and floor are 1–2 orders larger than that on the ceiling, which is in good agreement with the experimental and numerical results of (Sippola and Nazaroff 2003) and (Zhao and Chen 2006). In the normal direction, the deposition flux of 1 μm on the ceiling is nearly 5e–4, which is three-order larger than 10 μm. Same trends can also be observed in the other two wind directions. This is because gravitational settling dominates the movements of large particles, making more particles deposit on the vertical surfaces and floor. Conversely, small particles possessing relatively low Stokes number will follow the airflow tightly and disperse more uniformly. Furthermore, more particles with 10 μm deposit on the floor than 1 μm, but the difference is not conspicuous. Moreover,

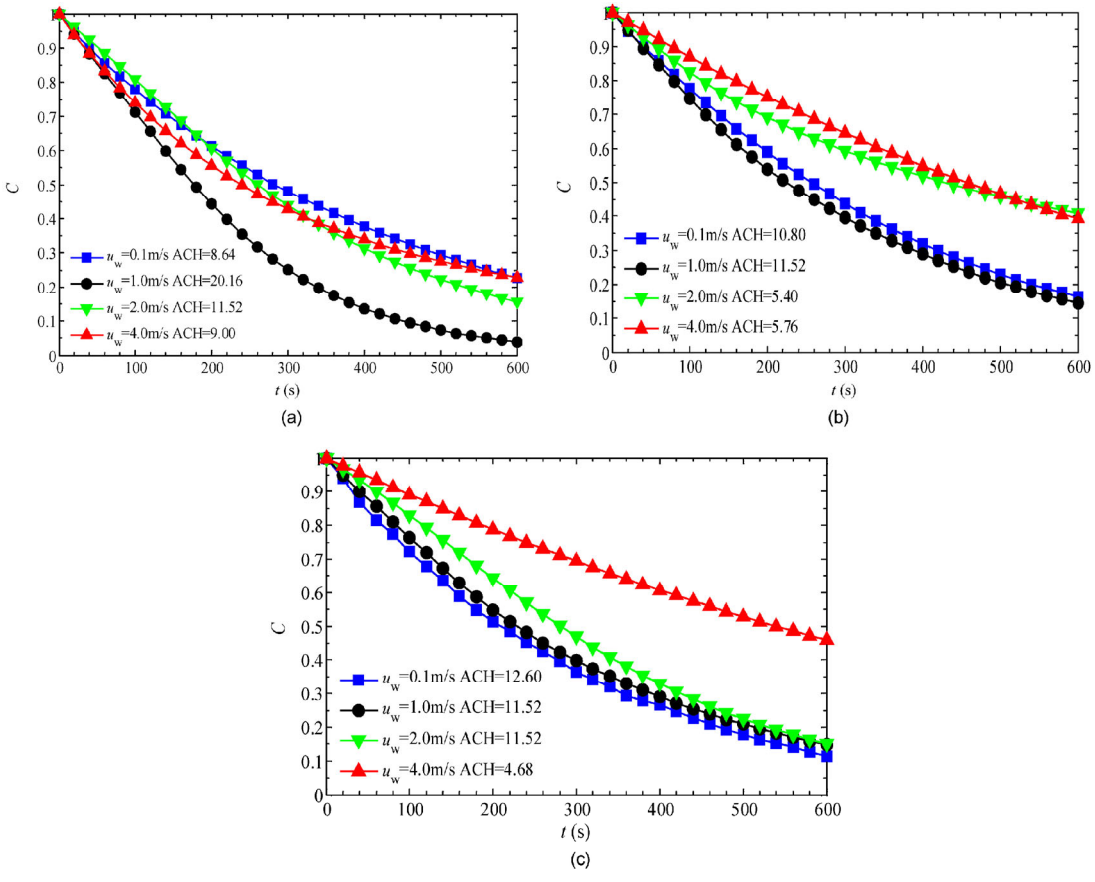

Fig. 12 Comparison of normalized average tracer gas concentration at four wind speeds and the corresponding ACH values in three directions: (a) normal direction; (b) left 45°; (c) right 45°

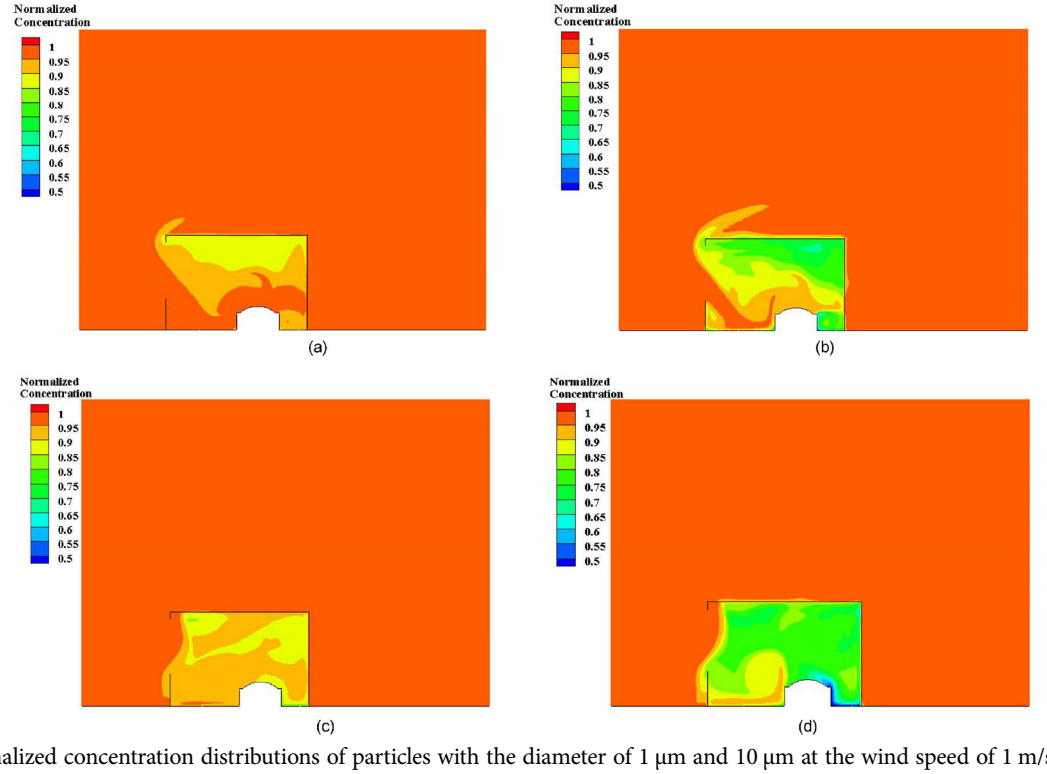

Fig. 13 Normalized concentration distributions of particles with the diameter of 1 μm and 10 μm at the wind speed of 1 m/s and 4 m/s in the normal wind direction. (a) 1 μm, 1 m/s; (b) 10 μm, 1 m/s; (c) 1 μm, 4 m/s; (d) 10 μm, 4 m/s

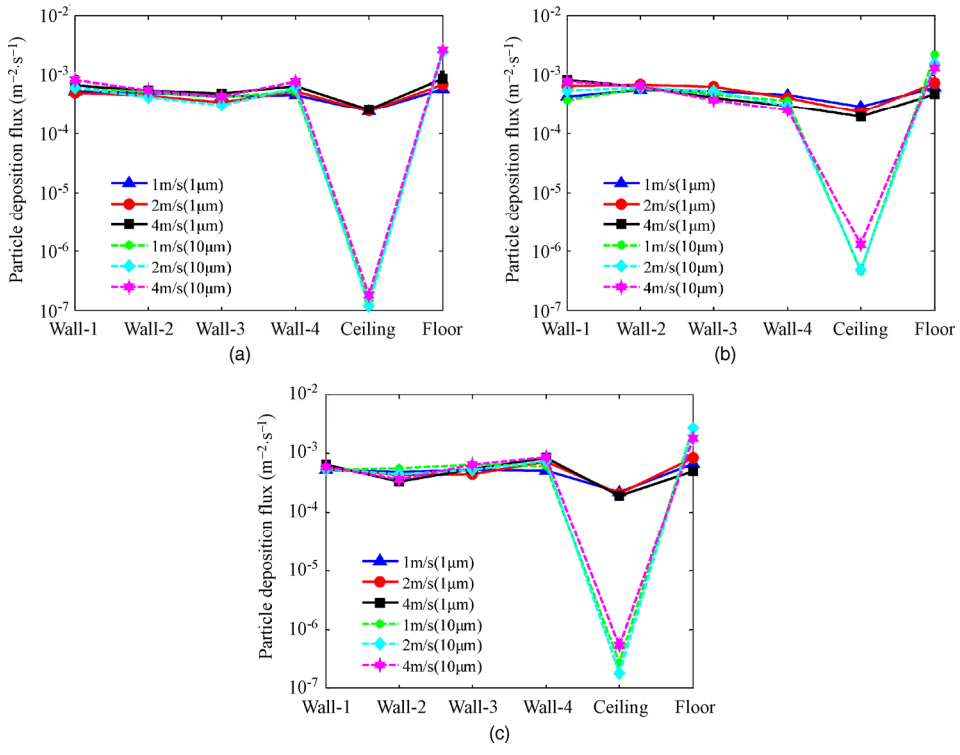

Fig. 14 Particle deposition flux on the surfaces of the room at the wind speeds of 1 m/s, 2 m/s and 4 m/s in three wind directions: (a) normal direction; (b) left 45°; (c) right 45°

the deposition flux varies little with the wind direction also, showing that the wind direction plays a non-significant role in the particle deposition.

Figure 15 shows the normalized average particle concentrations at various wind speeds and in three wind directions. It can be seen that large particles have lower concentrations than small particles at the same wind speed and in the same direction. Besides, the wind direction does have influence on the average concentration of particles especially at large wind speeds, because the non-normal wind direction and large wind speed can result in a strong mixing effect near the opening, restricting the particle entrance. When the wind speed is relatively small (1 m/s and 2 m/s), however, the average concentrations in three wind directions do not change a lot, showing that the effect of wind direction becomes not important at low wind speeds.

5 Conclusions

The Eulerian drift-flux model combined with Eulerian fluid model is employed in this study to predict the particle transport and airflow pattern in an isolated living room with single-sided natural ventilation.

For the airflow pattern, larger wind speed does not necessarily bring on a better ventilation effect and a higher ACH. The interfacial mixing effect at the opening is relatively

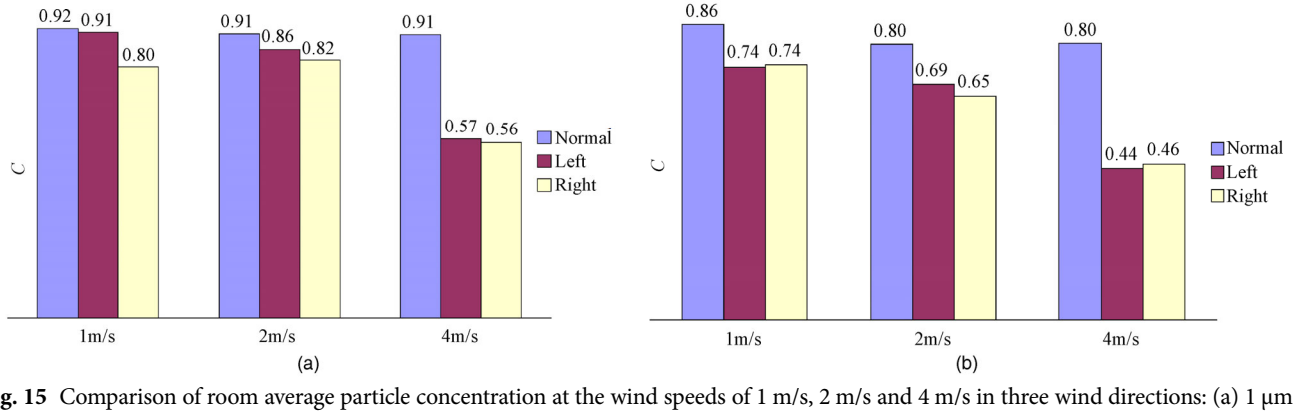

Fig. 15 Comparison of room average particle concentration at the wind speeds of 1 m/s, 2 m/s and 4 m/s in three wind directions: (a) 1 μm particle; (b) 10 μm particle

strong at high wind speeds, rendering less air entering into the room. As for the steady particle distribution, small particles tend to fill the room uniformly, yet stratified concentration pattern appears for the large particles. The deposition flux on the room surfaces varies little with wind speeds and directions. However, the deposition flux on the ceiling of large particle is three orders lower than that of small one, and the effect of wind direction on the room average concentration becomes conspicuous at high wind speeds.

For the single-sided natural ventilation, the indoor air quality is deeply affected by the outdoor particles, so more emphases should be placed on the natural ventilation optimization for the future studies.

Acknowledgements

The financial supports for this research, from the National Natural Science Foundation of China (Grant No. 51476055), are gratefully acknowledged.

References

Angel S, Parent J, Civco D, Blei A, Potere D (2011). The dimensions of global urban expansion: Estimates and projections for all countries, 2000–2050. *Progress in Planning*, 75: 53–107.

ANSYS (2012). ANSYS FLUENT 14 User's Guide.

Ayo SA, Mohd-Ghazali N, Mansor S (2015). Outdoor ventilation performance of various configurations of a layout of two adjacent buildings under isothermal conditions. *Building Simulation*, 8: 81–98.

Chen F, Yu SCM, Lai ACK (2006). Modeling particle distribution and deposition in indoor environments with a new drift-flux model. *Atmospheric Environment*, 40: 357–367.

Chen Y, Ebenstein A, Greenstone M, Li H (2013). Evidence on the impact of sustained exposure to air pollution on life expectancy from China's Huai River policy. *PNAS*, 110: 12936–12941.

Dockery DW, Pope CA, Xu X, Spengler JD, Ware JH, Fay ME, Ferris BG, Speizer FE (1993). An association between air pollution and mortality in six U.S. cities. *The New England Journal of Medicine*, 329: 1753–1759.

Etheridge D, Sandberg M (1996). Building Ventilation: Theory and Measurement. Chichester, UK: John Wiley & Sons.

Gao NP, Niu JL (2004). CFD study on micro-environment around human body and personalized ventilation. *Building and Environment*, 39: 795–805.

Gao NP, Niu JL, Perino M, Heiselberg P (2008). The airborne transmission of infection between flats in high-rise residential buildings: Tracer gas simulation. *Building and Environment*, 43:1805–1817.

da Graça GC, Chen Q, Glicksman LR, Norford LK (2002). Simulation of wind-driven ventilative cooling systems for an apartment building in Beijing and Shanghai. *Energy and Buildings*, 34: 1–11.

Hörschler I, Schröder W, Meinke M (2010). On the assumption of steadiness of nasal cavity flow. Journal of Biomechanics, 43: 1081–1085.

Hunt GR, Linden PP (1999). The fluid mechanics of natural ventilation-displacement ventilation by buoyancy-driven flows assisted by wind. *Building and Environment*, 34: 707–720.

Jiang Y, Alexander D, Jenkins H, Arthur R, Chen Q (2003). Natural ventilation in buildings: measurement in a wind tunnel and numerical simulation with large-eddy simulation. *Journal of Wind Engineering and Industrial Aerodynamics*, 91: 331–353.

Lai ACK, Chen FZ (2007). Comparison of a new Eulerian model with a modified Lagrangian approach for particle distribution and deposition indoors. *Atmospheric Environment*, 41: 5249–5256.

Lai ACK, Nazaroff WW (2000). Modeling indoor particle deposition from turbulent flow onto smooth surfaces. *Journal of Aerosol Science*, 31: 463–476.

Larsen TS, Heiselberg P (2007). Single-sided natural ventilation driven by a combination of wind pressure and temperature difference. In: Proceedings III of 6th International Conference on Indoor Air Quality, Ventilation & Energy Conservation in Buildings: Sustainable Built Environment, Sendai, Japan.

Launder BE, Spalding DB (1974). The numerical computation of turbulence flows. *Computing Methods Applied Mechanical Engineering*, 3: 269–289.

Li Y, Li X (2015). Natural ventilation potential of high-rise residential buildings in northern China using coupling thermal and airflow simulations. *Building Simulation*, 8: 51–64.

Lo LJ, Novoselac A (2013). Effect of indoor buoyancy flow on wind-driven cross ventilation. *Building Simulation*, 6: 69–79.

Nazaroff WW (2004). Indoor particle dynamics. *Indoor Air*, 14: 175–183.

Sippola MR, Nazaroff WW (2003). Experiments measuring particle deposition from fully developed turbulent flow in ventilation ducts. *Aerosol Science and Technology*, 38: 914–925.

Wilson DJ, Kiel DE (1990). Gravity driven counter flow through an open door in a sealed room. *Building and Environment*, 25: 379–388.

Zhao B, Chen JJ (2006). Numerical analysis of particle deposition in ventilation duct. *Building and Environment*, 41: 710–718.

Zhao B, Zeng J (2009). A simple model to study the influence of fluctuating airflow on the effective air exchange rate when using natural ventilation. *Building Simulation*, 2: 63–66.

Zhao B, Zhang Y, Li X , Yang X, Huang D (2004). Comparison of indoor aerosol particle concentration and deposition in different ventilated rooms by numerical method. *Building and Environment*, 39: 1–8.